Latin American Journal of Solids and Structures
www.lajss.org

Computational Modelling of RC Slabs Cracking with an Embedded Discontinuity Formulation

Abstract

This paper investigates the cracking process of reinforced concrete slabs subjected to vertical load, involving their crack pattern and the load-displacement capacity curve. Concrete was discretized with hexahedral finite elements with embedded discontinuities; whereas steel reinforcement was represented by 3D bar elements, placed along the edges of the solid elements, both kinds of elements have three degrees of freedom per node. The constitutive behaviour of concrete considers the softening deformation after reaching a failure surface, whereas the hardening of the reinforcing steel is represented by a 1D rate independent plasticity model with isotropic hardening. The coupling of solid and bar finite elements was validated with a reinforced concrete slab reported in the literature; other two slabs were also investigated showing their cracking patters at the top and at the bottom surfaces.

Keywords

Slabs, embedded discontinuities, damage, reinforced concrete.

Juárez-Luna G. [a, 1]
Tena-Colunga A. [a,2]
Ayala G. [b,3]

[a] Universidad Autónoma Metropolitana, San Pablo No. 180, Col. Reynosa Tamaulipas, 02200 México, D.F. Telephone: (55) 5318-9000-2229; Fax: (55)5318-9085;
[b] Instituto de Ingeniería, Universidad Nacional Autónoma de México, Av. Universidad No. 3000, Ciudad Universitaria, 04510 Coyoacán, México, D.F. Telephone: (55) 5623-3508.
[1] gjl@azc.uam.mx
[2] atc@ azc.uam.mx
[3] gayalam@ii.unam.mx

http://dx.doi.org/10.1590/1679-78251890

Received 02.02.2015
In Revised Form 17.07.2015
Accepted 21.08.2015
Available online 25.08.2015

1 INTRODUCTION

The study of collapse in concrete elements is an interest topic in engineering; particularly, the determination of the first crack load and the crack pattern. It is well known that concrete strength under compression is from 10 to 20 times greater than the strength under tension, as shown the experimental results reported by Kupfer and Gerstle (1973). In the way to collapse of reinforced concrete elements, their behaviour at the beginning is approximately linear elastic; next, cracking occurs. Then, crushing appears and finally, plasticity in reinforcing steel initiates, although struc-

tural collapse may occur before yielding of steel bars. Particularly, in clamped reinforced concrete slabs, cracking initiates on the top surface, then at the centre on the bottom surface, growing as the load increases; whereas in simple supported slabs, cracking initiates at the centre of the span on the bottom surface, growing to the edges (Juárez-Luna and Caballero-Garatachea 2014).

Laboratory tests have been perform to obtain the cracking paths and the moment coefficients of the rectangular slabs such as Bach and Graf (1915), who tested 52 simple supported slabs on their edges and 35 strips supported as beams, which were loaded until failure occurs. In these experimental tests, the displacements at some points of the slabs and the slopes at the centre of the edges were measured; also, the propagation of the cracks was registered as reported by Westergaard and Slater (1921). Afterwards, other experimental tests were performed as those reported by Casadei *et al.* (2005), Foster *et al.* (2004), Galati *et al.* (2008), Gamble *et al.* (1961), Girolami *et al.* (1970), Hatcher *et al.* (1960), Hatcher *et al.* (1961), Jirsa *et al.* (1962), Mayes *et al.* (1959), Vanderbilt (1961), among others. It is interested to say that these references are the basis of the research and applications of the current analysis and design of the rectangular slabs.

In the modelling of the reinforced concrete slabs, de Borst and Nauta (1985) applied the smeared crack model to study an axisymmetric slab under shear penetration, showing that cracking initiated at the bottom face of the slab and the corresponding cracking paths. Then, Kwak and Filippou (1990) modelled a square slab supported on its corners with a concentrated load at the centre of the span, obtained the load *vs.* displacement curve, which was congruent with experimental results reported by Jofriet and McNeice (1971) and Mcneice (1967); in the reported results by Kwak and Filippou (1990), neither the first crack load nor the cracking pattern was given. There were other proposals for modelling reinforced concrete slabs such as Gilbert and Warner (1978), Hand *et al.* (1973), Hinton *et al.* (1981), Lin and Scordelis (1975), Wang *et al.* (2013) among others, most of them used the smeared crack model.

There are some commercial software for modelling reinforced concrete elements such as ABAQUS (ABAQUS 2011), ANSYS (ANSYS 2010), DIANA (DIANA 2008), ATENA (Kabele *et al.* 2010), NLFEAS (Smadi and Belakhdar 2007), among others. These software mainly use the finite element method with the smeared crack model for the behaviour of the concrete, equipped with a failure surface with different threshold value in tension and compression, necessary to determine the first crack load and crack propagation. However, the smeared crack model may have numerical problems of stress locking and spurious kinematic modes (Rots 1988), which may be overcome with heuristic shear retention factors.

In this paper, finite elements with embedded discontinuities (FEED) were used for studying reinforced concrete slabs, computing their load-displacement capacity curves and their cracking patterns. The advantages of FEED are the capability for representing highly localized strains by improving the kinematic, the possibility to statically condense out the displacement jump and the nearly mesh-independent. Concrete was discretized with hexahedral FEED and steel reinforcement was discretized with 3D bar elements, both kinds of elements have three degrees of freedom per node.

The outline of this paper is as follows. Section 2 presents the details of FEED formulation. Section 3 provides the constitutive models to describe the behaviour of the materials, a discrete damage

model equipped with softening for concrete and a plasticity model for the steel reinforcement. Numerical examples of reinforce concrete slabs which validate the proposed formulation are presented in Section 4. Finally, in Section 5, conclusions derived from this work are given.

2 EMBEDDED DISCONTINUITY MODEL

2.1 Variational formulation

The FEED are formulated from an energy functional which has the displacement, $\mathbf{u}$, and the displacement jump $[|\mathbf{u}|]$ as independent variable (Alfaiate *et al.* 2003, Juárez and Ayala 2009, Lotfi and Shing 1995, Wells and Sluys 2001). This functional is given by:

$$\Pi\left(\mathbf{u},[\left|\mathbf{u}\right|]\right) = \int_{\Omega\setminus S}\left[\Psi(\overline{\boldsymbol{\varepsilon}}^{u}) - \mathbf{b}\cdot\mathbf{u}\right]d\Omega - \int_{\Gamma_{\sigma}}\mathbf{t}^{*}\cdot\mathbf{u}\,d\Gamma + \int_{\Gamma_{S}}\phi_{S}([\left|\mathbf{u}\right|])d\Gamma \tag{1}$$

where the free energy density, $\Psi(\overline{\boldsymbol{\varepsilon}}^{u})$, depends on the continuous strain field $\overline{\boldsymbol{\varepsilon}}^{u}$, and the free discrete energy density, $\Psi_{S}([\left|\mathbf{u}\right|])$, depends on the displacement jump. These energy densities are respectively given by:

$$\Psi(\overline{\boldsymbol{\varepsilon}}^{u}) = \int_{0}^{\overline{\boldsymbol{\varepsilon}}}\boldsymbol{\sigma}(\overline{\boldsymbol{\varepsilon}})d\overline{\boldsymbol{\varepsilon}} \tag{2}$$

$$\phi_{S}([\left|\mathbf{u}\right|]) = \int_{0}^{[|\mathbf{u}|]}\mathbf{T}_{S}([\left|\mathbf{u}\right|]_{n,s})d[\left|\mathbf{u}\right|] \tag{3}$$

where the elastic stresses, $\boldsymbol{\sigma}$, are defined by:

$$\boldsymbol{\sigma} = \mathbf{C} : \overline{\boldsymbol{\varepsilon}} \tag{4}$$

and $\mathbf{T}_{\mathrm{S}}$ is the traction vector at the discontinuity.

2.2 Finite Element Approximation

It is not possible to prescribe the boundary conditions, $\mathbf{u}^{*}$, in only one of the displacement fields, *i.e.*, $\overline{\mathbf{u}}$ or $[|\mathbf{u}|]$, a difficulty overcame, according to Oliver (1996), defining the displacement as in Eq. (5), shown in Figures 1a and b:

$$\mathbf{u} = \hat{\mathbf{u}} + M_{S}(\mathbf{x})[\left|\mathbf{u}\right|] \tag{5}$$

Then, the strain field is defined by:

$$\boldsymbol{\varepsilon} = \nabla^{S}\mathbf{u} = \nabla^{S}\hat{\mathbf{u}} + \nabla^{S}M_{S}(\mathbf{x})[\left|\mathbf{u}\right|] \tag{6}$$

where $\hat{\mathbf{u}}$ is the regular displacement field and $M_{S}(\mathbf{x})$ is a function given by:

$$M_S(\mathbf{x}) = H_S(\mathbf{x}) - \phi(\mathbf{x}) \tag{7}$$

where $\phi(\mathbf{x})$ is a continuous function such that:

$$\begin{aligned} \phi(\mathbf{x}) &= 0 \quad \forall \mathbf{x} \in \Omega^- \\ \phi(\mathbf{x}) &= 1 \quad \forall \mathbf{x} \in \Omega^+ \end{aligned} \tag{8}$$

The function M_S, has two properties: $M_S(x) = 1 \quad \forall x \in S$ and $M_S(x) = 0 \quad \forall x \in \Omega^- \cup \Omega^+$ as shown in
Figure **1**.

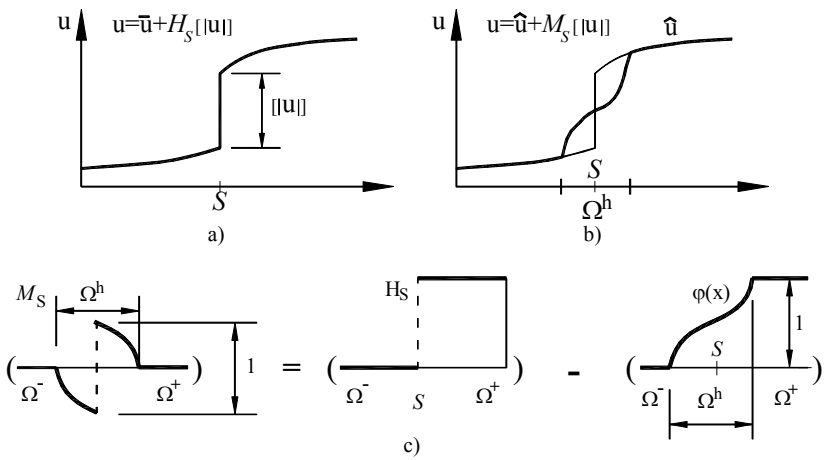

Figure 1: Graphic representation of: a) continuous, b) regular displacements and c) function M_S.

The continuous displacement field is defined as:

$$\bar{\mathbf{u}} = \hat{\mathbf{u}} - \phi(\mathbf{x})\left[\left|\mathbf{u}\right|\right] \tag{9}$$

In the continuous part of the solid, which may be linear elastic, the continuous strain field, $\bar{\boldsymbol{\varepsilon}}$ is given by:

$$\bar{\boldsymbol{\varepsilon}} = \nabla^S \bar{\mathbf{u}} \tag{10}$$

Substituting Eq. (9) into Eq. (10),

$$\bar{\boldsymbol{\varepsilon}} = \nabla^S \hat{\mathbf{u}} - \nabla^S \phi(\mathbf{x})\left[\left|\mathbf{u}\right|\right] - \phi(\mathbf{x})\nabla^S\left[\left|\mathbf{u}\right|\right] \tag{11}$$

If the displacement jump is constant in Eq. (11), the continuous strain field may be rewritten as:

$$\bar{\boldsymbol{\varepsilon}} = \nabla^S \hat{\mathbf{u}} - \nabla^S \phi(\mathbf{x})\left[\left|\mathbf{u}\right|\right] \tag{12}$$

2.3 Approximation of the Displacement and Strain Fields

The regular displacement field is approximated by:

$$\hat{\mathbf{u}} = \mathbf{N}\mathbf{d} \tag{13}$$

where $\mathbf{N}$ is the standard vector of shape functions of the element

$$\mathbf{N} = \sum_{i=1}^{i=n} N_i^{(e)} \tag{14}$$

and, $\mathbf{d}$, is the nodal displacement vector. The function, $M_S(\mathbf{x})$, is defined in the finite element approximation as:

$$M_S^e(\mathbf{x}) = H_S^e\left(\mathbf{x}\right) - \phi^e \tag{15}$$

where ϕ^e is constructed by:

$$\phi^e = \sum_{i^+=1}^{n_e^+} N_{i^+} \tag{16}$$

where N_{i^+} are the shape functions corresponding to the nodes placed on Ω^+ of the finite element which contains the discontinuity, in agreement with the definition of ϕ in Eq. (8).

The displacement field defined in Eq. (5) is given by

$$\mathbf{u} = \mathbf{N}\mathbf{d} + \underbrace{M_S^e}_{\mathbf{N}_c}\left[\left|\mathbf{u}\right|\right]_{x,y} \tag{17}$$

The continuous strain field in Eq. (12) is approximated as:

$$\overline{\boldsymbol{\varepsilon}} = \mathbf{B}\cdot\mathbf{d} - \underbrace{\nabla\phi^e}_{\mathbf{B}_c}\cdot\left[\left|\mathbf{u}\right|\right]_{x,y} \quad \forall\mathbf{x}\in\Omega\ /\ S \tag{18}$$

where $\mathbf{B}$, is the standard strain interpolation matrix, containing the derivatives of the standard shape functions $\partial(\mathbf{N}\mathbf{d}) = \mathbf{B}\mathbf{d}$.

The equilibrium equations corresponding to this formulation are obtained by substituting Eqs. (17) and (18) into the energy functional of Eq. (1), and setting the derivatives with respect to the independent variables ($\mathbf{d}$ and $[|\mathbf{u}|]$) to zero,

$$\frac{\partial\Pi}{\partial\mathbf{d}} = 0 = \int_{\Omega\setminus S}\mathbf{B}^T\boldsymbol{\sigma}\left(\overline{\boldsymbol{\varepsilon}}\right)d\Omega - \int_{\Omega}\mathbf{N}^T\cdot\mathbf{b}\,d\Omega - \int_{\Gamma_\sigma}\mathbf{N}^T\cdot\mathbf{t}^*d\Gamma \tag{19}$$

$$\frac{\partial\Pi}{\partial\left[\left|\mathbf{u}\right|\right]} = 0 = -\int_{\Omega\setminus S}\mathbf{B}_c^T\boldsymbol{\sigma}\left(\overline{\boldsymbol{\varepsilon}}\right)d\Omega + \int_{\Gamma_S}\mathbf{T}_{x,y}d\Gamma \tag{20}$$

In Eqs. (19) and (20), $\boldsymbol{\sigma}\left(\overline{\boldsymbol{\varepsilon}}\right)$ and $\mathbf{T}_{x,y,z}$ are nonlinear, their respective linearizations with Taylor series give (Juárez-Luna and Ayala 2014):

$$\begin{bmatrix} \int_{\Omega\setminus S}\mathbf{B}^{\mathbf{T}}\cdot\mathbf{C}\cdot\mathbf{B}d\Omega & -\int_{\Omega\setminus S}\mathbf{B}^{\mathbf{T}}\cdot\mathbf{C}\cdot\mathbf{B}_c d\Omega \\ -\int_{\Omega\setminus S}\mathbf{B}_c^{\mathbf{T}}\cdot\mathbf{C}\cdot\mathbf{B}d\Omega & -\int_{\Omega\setminus S}\mathbf{B}_c^{\mathbf{T}}\cdot\mathbf{C}\cdot\mathbf{B}_c d\Omega+\int_{\Gamma_S}\mathbf{R}^T\cdot\mathbf{T}\cdot\mathbf{R}d\Gamma \end{bmatrix}^{(n,0)} \begin{Bmatrix} \Delta d \\ \Delta\left[\left|\mathbf{u}\right|\right]_{x,y} \end{Bmatrix}^{(n,1)} = \begin{Bmatrix} R_1 \\ R_2 \end{Bmatrix}^{(n,0)} \quad (21)$$

where $\mathbf{R}$ has the direction cosines, R_1 and R_2 are defined as:

$$R_1 = F_{ext}^{(n)} - \int_{\Omega\setminus S}\mathbf{B}^T\boldsymbol{\sigma}\left(\overline{\boldsymbol{\varepsilon}}\right)d\Omega^{(n,0)} \quad (22)$$

$$R_2 = \int_{\Omega\setminus S}\mathbf{B}_c^T\boldsymbol{\sigma}\left(\overline{\boldsymbol{\varepsilon}}\right)d\Omega^{(n,0)} - \int_{\Gamma_S}\mathbf{T}_{x,y}d\Gamma^{(n,0)} \quad (23)$$

To reduce the size of the system given in Eq. (21), the additional degrees of freedom, $\Delta[|\mathbf{u}|]$, may be condensed. In Eq. (22), R_1 means the equilibrium between the external and the internal forces in the domain $\Omega \setminus S$, whereas R_2, in Eq. (23), the equilibrium between the forces in the domain $\Omega \setminus S$ and forces in the discontinuity Γ_S.

Tractions at the discontinuity are:

$$\mathbf{T}_{x,y,z} = \frac{1}{A_d}\int_{\Omega\setminus S}\mathbf{B}_c^T\boldsymbol{\sigma}d\Omega \quad (24)$$

which expressed in the local system becomes

$$\mathbf{T}_{n,s,t} = \frac{1}{A_d}\mathbf{R}\int_{\Omega\setminus S}\mathbf{B}_c^T\boldsymbol{\sigma}d\Omega \quad (25)$$

The definitions of the traction vector in Eqs. (24) and (25) are dependent on the discontinuity area, A_d, and the direction cosines to the normal vector $\mathbf{n}$, as shown in Figure 2.

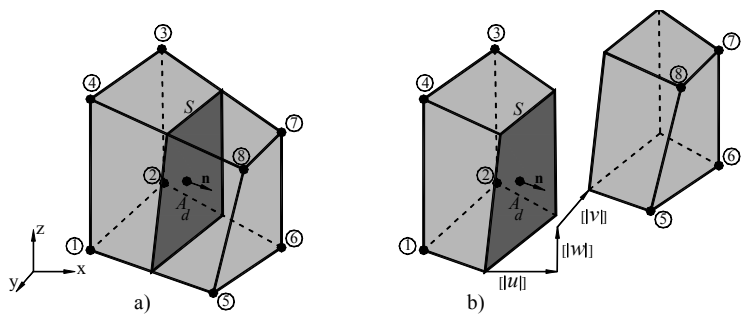

Figure 2: Finite element: a) discontinuity area and b) displacement jumps.

The FEED, given in eq. (21), were implemented in the finite element analysis program (FEAP), developed by Taylor (2008). These FEED capture a discontinuity surface at their geometric centre, which is placed perpendicular to the major principal stress direction. The discontinuity sur-

faces of the surrounding elements are not aligned as Sancho *et al.* (2007) did for 2D problems. Although there are formulations which consider linear displacement jumps inside the element such as Alfaiate *at al.* (2003) and Contrafatto *et al.* (2012), the displacement jump is constant into these FEED. It is important to say that these elements do not have problems of spurious shear deformations and they satisfied the following requirements: (1) equilibrium, traction continuity across the discontinuity interface and (2) kinematics, free relative rigid body motions of the two portions of an element split up by a discontinuity (Juárez-Luna and Ayala 2014).

3 CONSTITUTIVE MODELS

3.1 Concrete

The concrete behaviour was modelled with a discrete damage model, which has different threshold values under tension and compression, as shown in Figure 3a. This model is equipped with softening after reaching the ultimate tensile strength, T_{ut}, or the ultimate compressive strength, T_{uc}, shown in Figure **3**b. This model is defined by the following equations:

$$
\begin{aligned}
&\text{Discrete free energy density} && \phi\left(\left[\left|\mathbf{u}\right|\right],\bar{\alpha}\right)=\left(1-\omega\right)\phi_0\left(\bar{\alpha}\right),\begin{cases}\phi_0\left(\left[\left|\mathbf{u}\right|\right]\right)=\frac{1}{2}\left[\left|\mathbf{u}\right|\right]\cdot\mathbf{Q^e}\cdot\left[\left|\mathbf{u}\right|\right]\\ \mathbf{Q^e}=\mathbf{n}\cdot\mathbf{C}\cdot\mathbf{n}\end{cases}\\
&\text{Constitutive equation} && \mathbf{T}=\frac{\partial\phi\left(\left[\left|\mathbf{u}\right|\right],\bar{\alpha}\right)}{\partial\left[\left|\mathbf{u}\right|\right]}=(1-\omega)\mathbf{Q^e}\cdot\left[\left|\mathbf{u}\right|\right]\\
&\text{Damage variable} && \omega=1-\frac{\bar{q}\left(\bar{\alpha}\right)}{\bar{\alpha}};\quad \omega\in\left[-\infty,1\right]\\
&\text{Evolution law} && \dot{\bar{\alpha}}=\dot{\bar{\lambda}}=\frac{\partial}{\partial t}\left(\bar{\alpha}\right),\quad \bar{\alpha}\in\left[0,\infty\right]\\
&\text{Damage criterion} && f(\mathbf{T},\bar{q})=\tau_{\mathbf{T}}-\bar{q};\quad \tau_{\mathbf{T}}=\left\|\mathbf{T}\right\|_{\mathbf{Q^{e-1}}}=\sqrt{\mathbf{T}\cdot\mathbf{Q^{e^{-1}}}\cdot\mathbf{T}}\\
&\text{Hardening rule} && \dot{\bar{q}}\left(\bar{\alpha}\right)=\bar{H}\,\dot{\bar{\alpha}};\qquad \bar{H}=\bar{q}^{'}\left(\bar{\alpha}\right)\leq 0\\
&\text{Loading-unloading conditions} && f\leq 0;\qquad \dot{\bar{\lambda}}\geq 0;\qquad \dot{\bar{\lambda}}f=0;\qquad \dot{\bar{\lambda}}\dot{f}=0\ \text{(consistency)}
\end{aligned}
\tag{26}
$$

where ϕ is the discrete free energy density, $\mathbf{T}$ is the traction vector. The damage variable ω is defined in terms of the hardening/softening variable $\dot{\bar{q}}$, which is dependent on the hardening/softening parameter. The damage multiplier $\dot{\bar{\lambda}}$ determines the loading-unloading conditions, the function $f(\mathbf{T},\bar{q})$, bounds the elastic domain defining the damage surface in the tractions space. The tangent constitutive equation, in terms of rates from the model in Eq. (26), is:

$$
\dot{\mathbf{T}}=\mathbf{C}_d^T\cdot\left[\left|\dot{\mathbf{u}}\right|\right] \tag{27}
$$

where $\mathbf{C}_d^T$ is the tangent constitutive operator, relating the traction and the displacement jump of the nonlinear loading interval, which is defined by

$$
\mathbf{C}_d^T=\left(1-\omega\right)\mathbf{Q^e}-\frac{\bar{q}-\bar{H}\bar{\alpha}}{\bar{\alpha}^3}\left(\mathbf{Q^e}\cdot\left[\left|\mathbf{u}\right|\right]\otimes\left[\left|\mathbf{u}\right|\right]\cdot\mathbf{Q^e}\right) \tag{28}
$$

and for the elastic loading and unloading interval ($\dot{d} = 0$ and $\dot{\omega} = 0$):

$$\mathbf{C}_d^T = \left(1-\omega\right)\mathbf{Q}^{\mathbf{e}} \tag{29}$$

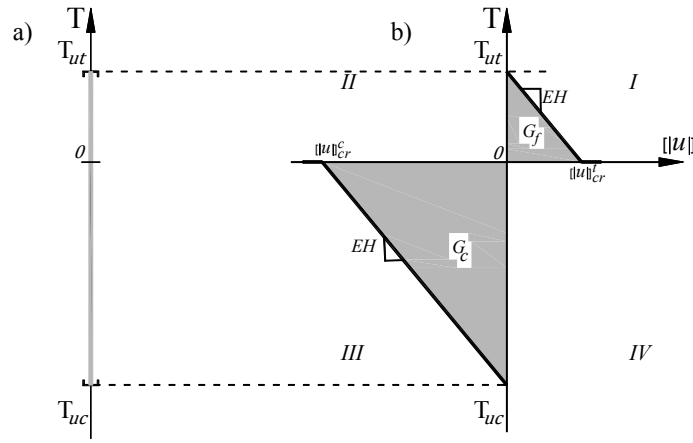

Figure 3: 1D discrete damage model with softening: a) elastic space and b) traction-displacement jump curve.

This constitutive model considers a material fictitious interpenetration, $[|\mathbf{u}|]^c$, when T_{uc} is overcome. Because of the energy dissipation in compression takes place over a surface, rather than within a volume, the use of a fictitious interpenetration instead of a strain is justified (Carpinteri *et al.* 2010). In this model, it is assumed that both post-peak regimes, tension and compression, have decreasing functions with the same slope, *EH,* as ca be seen in Figure **3**b.

The area under the traction versus jump displacement curve represents the fracture energy density, G_f , in the first quadrant of Figure **3**b, *i.e.*:

$$G_f = \frac{1}{2}\mathrm{T}_{ut}\left[\left|u\right|\right]_{cr}^{t} \tag{30}$$

where $[|\mathbf{u}|]_{cr}^{t}$ is the critical value of the crack opening, which is given by:

$$\left[\left|u\right|\right]_{cr}^{t} = -\frac{\mathrm{T}_{ut}}{EH} \tag{31}$$

Substituting Eq. (31) into Eq. (30) and solving for *EH*, the slope of the decreasing function under tension is given by:

$$EH = -\frac{1}{2}\frac{\mathrm{T}_{ut}^2}{G_f} \tag{32}$$

Considering that the area under the compression versus the fictitious jump interpenetration displacement curve represents the crushing energy density, G_c , in the third quadrant of Figure **3**b, then

$$G_c = \frac{1}{2} \mathrm{T}_{uc} \left[\left| u \right| \right]_{cr}^{c} \tag{33}$$

The fictitious critical value of interpenetration can be computed as:

$$\left[\left| u \right| \right]_{cr}^{t} = -\frac{\mathrm{T}_{uc}}{EH} \tag{34}$$

Substituting Eq. (34) into Eq. (33), then:

$$G_c = -\frac{1}{2} \frac{\mathrm{T}_{uc}^2}{EH} \tag{35}$$

As the slope of the decreasing function under tension is the same under compression, Eq. (32) is substituted into Eq. (35):

$$G_c = \frac{\mathrm{T}_{uc}^2}{\mathrm{T}_{ut}^2} G_f \tag{36}$$

If n= T_{ut} / T_{uc} in Eq.(36), G_c is given by:

$$G_c = n^2 G_f \tag{37}$$

This equation provides a relationship between the crushing and the fracture energy densities.

3.2 Steel

A 1D rate independent plasticity model with isotropic hardening was used for modelling the steel reinforcement. This model has the same threshold value in tension and compression, as shown in Figure 4a; the hardening of the steel reinforcement, after reaching the yield stress σ_y, was considered with an idealized bilinear function as shown in Figure 4b. The plasticity model is defined by the following equations:

Free energy density	$\Psi\left(\boldsymbol{\varepsilon}, r\right) = \frac{1}{2}\boldsymbol{\varepsilon}:\mathbf{C}:\boldsymbol{\varepsilon} + \Psi^p\left(\alpha\right)$
Constitutive equation	$\boldsymbol{\sigma} = \frac{\partial \Psi}{\partial \boldsymbol{\varepsilon}} = \mathbf{C} : \left(\boldsymbol{\varepsilon} - \boldsymbol{\varepsilon}^p\right)$
Plastic variable	$\alpha = \partial\lambda_{\sigma_y} H\left(\sigma_y\right) = \lambda; \quad \alpha \in \left[0, \infty\right]$
Evolution law	$\dot{\boldsymbol{\varepsilon}}^p = \lambda \frac{\partial f}{\partial \sigma}$
Yield function	$f(\boldsymbol{\sigma}, \boldsymbol{\sigma}_y) = F\left(\boldsymbol{\sigma}\right) - \boldsymbol{\sigma}_y = 0$
Hardening rule	$\sigma_y = h\left(\boldsymbol{\varepsilon}^p\right) \rightarrow h\left(\boldsymbol{\varepsilon}^p\right) = \frac{\partial \Psi^p\left(\alpha\right)}{\partial \alpha}$ $h'\left(\boldsymbol{\varepsilon}^p\right) = H\left(\boldsymbol{\varepsilon}^p\right) \rightarrow H\left(\boldsymbol{\varepsilon}^p\right) = \sigma_y' = \frac{\partial^2 \Psi^p\left(\alpha\right)}{\partial \alpha^2}$
Loading-unloading conditions	$f \leq 0; \quad \dot{\lambda} \geq 0; \quad \dot{\lambda} f = 0; \quad \bar{\lambda} \dot{f} = 0$ (consistency)

(38)

where ψ is the free energy density, $\boldsymbol{\sigma}$ is the stress tensor. The plastic variable α is defined in terms of the hardening variable H. The plastic multiplier λ determines the loading-unloading con-

ditions, the function $f(\boldsymbol{\sigma},\boldsymbol{\sigma}_y)$, bounds the elastic domain defining the plastic surface in the stress space. The tangent constitutive equation, in terms of rates from the model in Eq. (38), is:

$$\dot{\boldsymbol{\sigma}} = \mathbf{C}^T : \dot{\boldsymbol{\varepsilon}} \tag{39}$$

where $\mathbf{C}^T$ is the tangent constitutive operator, relating the stresses and the strain of the nonlinear loading interval, which is defined by

$$\mathbf{C}^T = \mathbf{C} - \frac{\mathbf{C} : \mathbf{m} \otimes \mathbf{n} : \mathbf{C}}{H + \mathbf{n} : \mathbf{C} : \mathbf{m}} \tag{40}$$

and for the elastic loading and unloading interval ($\dot{\lambda} = 0$ and $\dot{\alpha} = 0$):

$$\mathbf{C}^T = \mathbf{C} \tag{41}$$

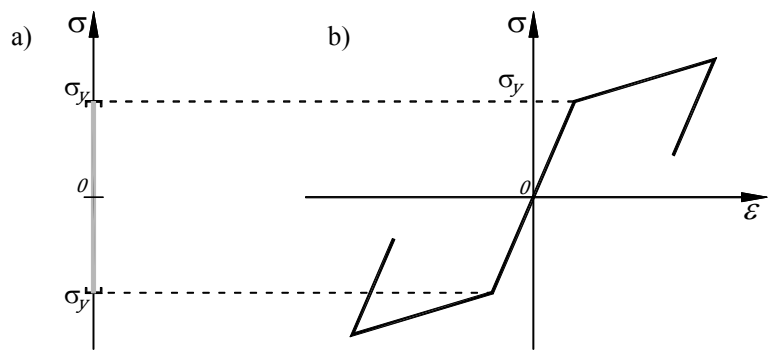

Figure 4: 1D rate independent plasticity model with isotropic hardening: a) elastic space and b) stress-strain curve.

4 NUMERICAL EXAMPLES

In the presented examples, the reinforcement was meshed with 3D linear finite elements with two nodes, which have three degrees of freedom each. The constitutive behaviour of the steel reinforcement was modelled with a plasticity model with hardening. The steel elements were placed on the edges of the solid elements, coupling the degree of freedom of both kinds of elements. Perfect bond between steel bars and concrete was assumed, as the failure of this type of slabs occurs mainly on flexure without evidence of debonding.

4.1 Square Slabs Supported at the Corners

The FEED and the constitutive models were validated by the numerical modelling of the experimental results reported by Girolami *et al.* (1970). The test specimen, shown in Figure 5a, is a square slab of sides 1.829 m long and a thickness 0.044 m, which was simple supported at its cor-

ners. The top and bottom reinforcement used in the slab consisted of 3.66 mm diameter steel bars cut from No.7 gage wire, which were spaced 10.954 cm in both orthogonal directions, as shown in Figure **6**a. Also, the stirrups were bent from the No.7 gage steel wire as shown in Figure **6**b. The vertical loads were applied at the top of the slab using four jacks with loading trees distributed to 16 load plates, as shown in Figure 5b. The mechanical properties of the concrete are: Young´s modulus E_c=19.90 GPa, Poisson ratio υ=0.2, ultimate tensile strength σ_{tu}=3.1026 MPa, ultimate compressive strength σ_{uc}=31.026 MPa and fracture energy density G_f=0.098 N/mm. The mechanical properties of the reinforcing steel are: Young´s modulus E_s=206 GPa, Poisson ratio υ=0.3, yield stress σ_y=330.95 MPa and hardening modulus H=2.871GPa.

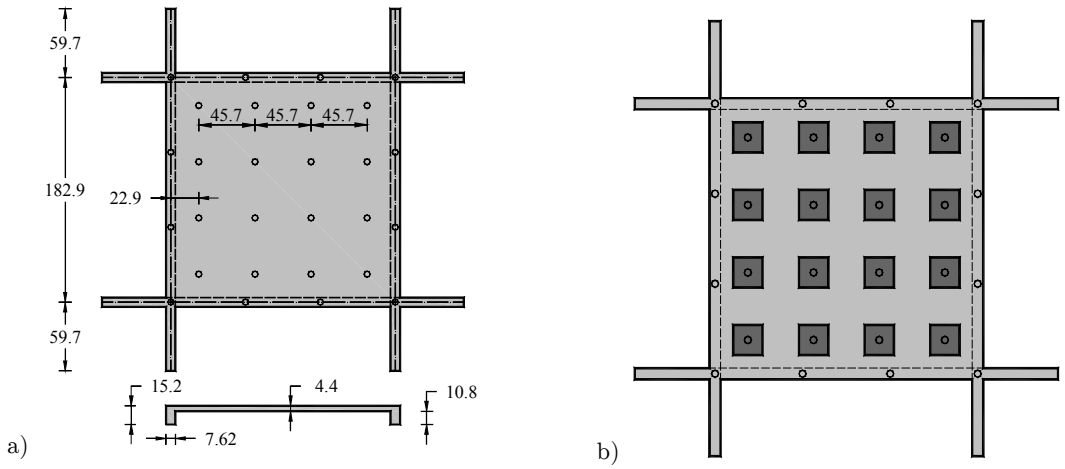

Figure 5: Experimental test: a) geometry in cm and b) applied loads (adapted from Girolami *et al.* 1970).

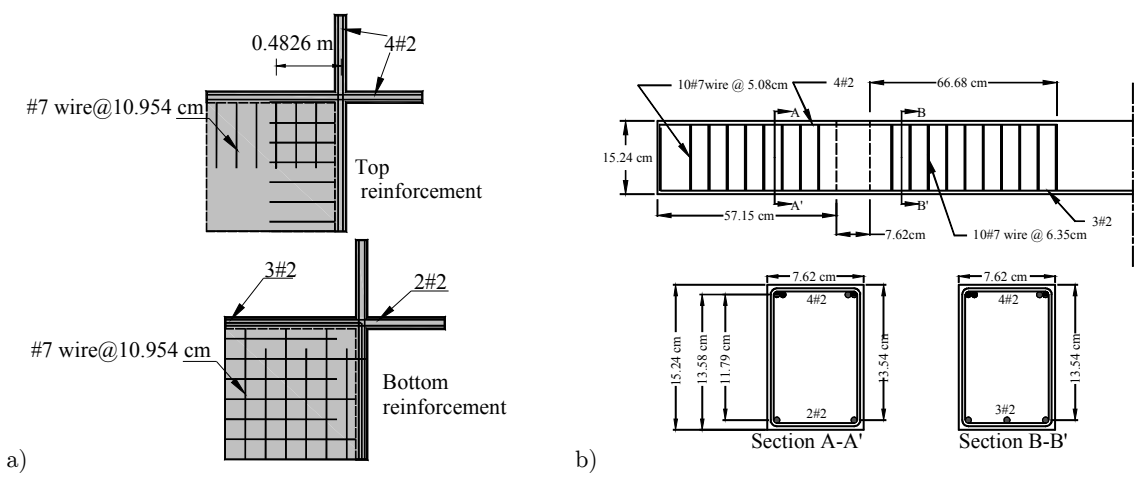

Figure 6: Reinforcement of: a) one quarter of the slab and b) one half of a beam (adapted from Girolami *et al.* 1970).

Only one quarter of the slab was modelled, considering the two axes of symmetry of its geometry. To describe the symmetry conditions at the boundary constraints, no translation was imposed on the degree of freedoms perpendicular to the corresponding axes of symmetry. The steel reinforcement mesh is shown in Figure 7a, whereas the concrete mesh of the slab and beams is shown in Figure 7b.

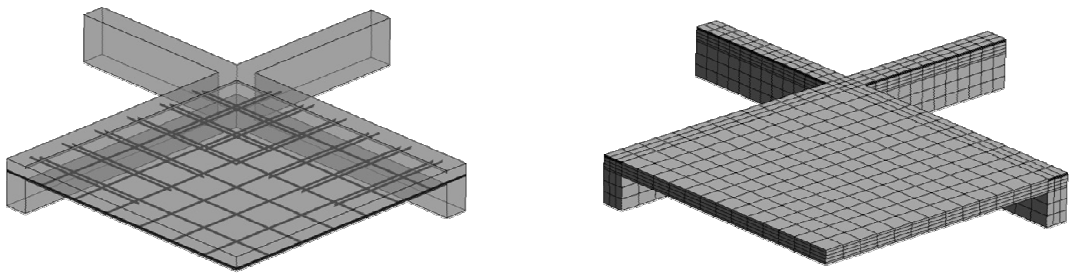

a) b)

Figure 7: Meshes: a) steel reinforcement in the slab and b) concrete.

The load *vs* displacement at the centre of the span curves are shown in Figure 8. The computed curve with FEED shows numerical results, which are congruent with the experimental curve reported by Girolami *et al.* (1970). In fact, it is observed that both curves are similar at the beginning; however, there is a backward of the displacement. This movement may be attributed to a sliding of the measurement devices, considering that the displacement at the centre would never move upwards as the load is applied downwards; this effect only happens at plain concrete elements such as beams, where snapback behaviour may occur (Carpinteri 1988). It is important to show that the numerical and the experimental curves are greater than the horizontal curve computed with the yield line theory. The yield line theory is a method to estimate the ultimate load of a slab system by postulating a collapse mechanism compatible with the boundary conditions. The moments at the plastic hinge lines are the ultimate moments of resistance of the sections, and the ultimate load is determined using the principle of virtual work or the equations of equilibrium (Park and Gamble 2000).

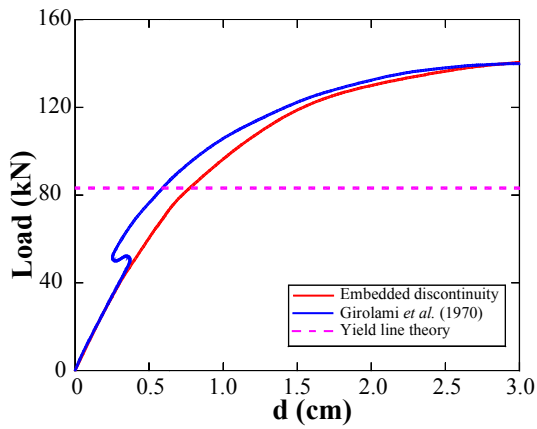

Figure 8: Comparison between experimental and numerical results.

Cracking initiated at the corners on the top surface, growing along the edges to the centre as shown in Figure 9a; on the bottom surface, cracking occurs at the centre, growing to the corner as shown in Figure 9b. The crack patterns at both, top and bottom surfaces, are congruent with the experimental results reported by Girolami *et al.* (1970).

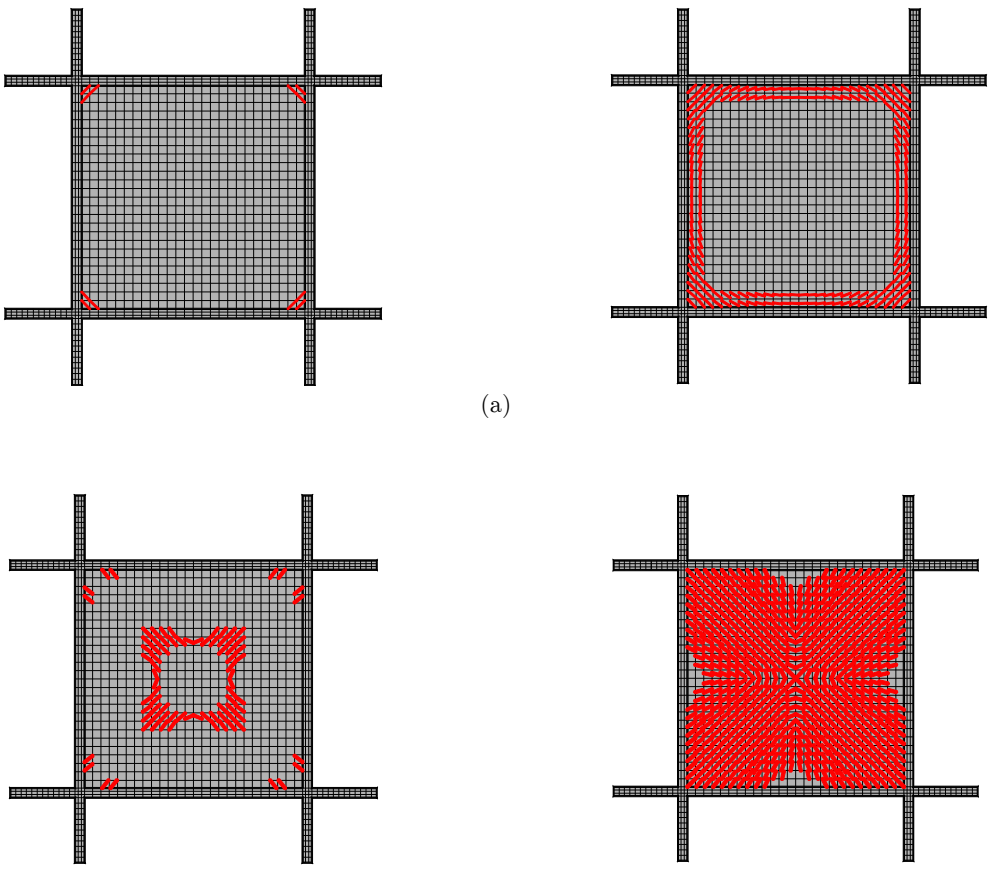

(a)

(b)

Figure 9: Cracking propagation on the: a) top and b) bottom surface.

4.2 Simple Supported and Clamped Slabs

Other two slabs were also analysed, a 4m square slab and a 2m width by 4m length rectangular slab respectively shown in Figure 10; both of them were 10 cm thick and subjected to an increasing uniform distributed load. Two boundary conditions were considered along their edges: simply supported and clamped. The reinforcement used in the slabs consisted of 3/8 in diameter steel bars, which were spaced 20 cm in both orthogonal directions, as shown respectively in Figures **11** and **12**. The mechanical properties of the concrete are: Young's modulus E_c=14710 MPa, Poisson ratio ν=0.2, ultimate tensile strength σ_{tu}=2.86 MPa, ultimate compressive strength σ_{cu}=28.63 MPa, fracture energy density G_f=0.098 N/mm. The mechanical properties of the steel reinforcement are: Young's modulus E_s=196.13 GPa, yield stress σ_y=411.88 MPa, Poisson ratio ν=0.3,

area A=0.71 cm^2 and hardening modulus H=2.871 GPa. Like the previous example, the two axes or symmetry were considered, so only a quarter of the slab was modelled, as shown in Figure 13, which reduces the time consuming of the computational calculation.

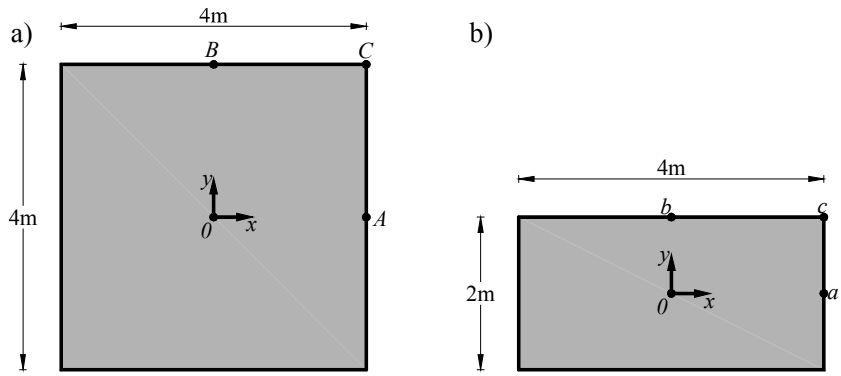

Figure 10: Geometry of slabs: a) square and b) rectangular.

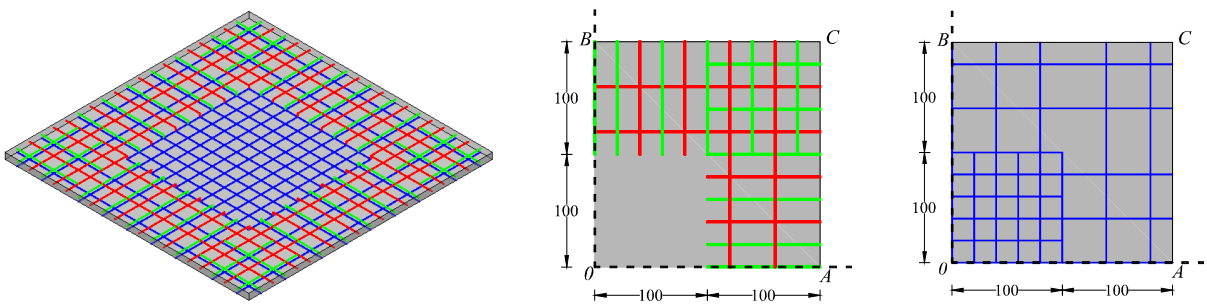

(a) (b) (c)

Figure 11: Steel reinforcement of the square slab: a) 3D view, b) first quadrant with top reinforcement and b) first quadrant with bottom reinforcement.

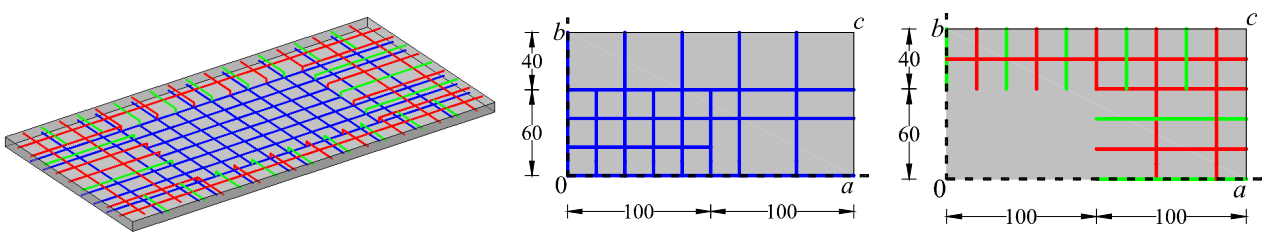

(a) (b) (c)

Figure 12: Steel reinforcement of the square slab: a) 3D view, b) first quadrant with top reinforcement and b) first quadrant with bottom reinforcement.

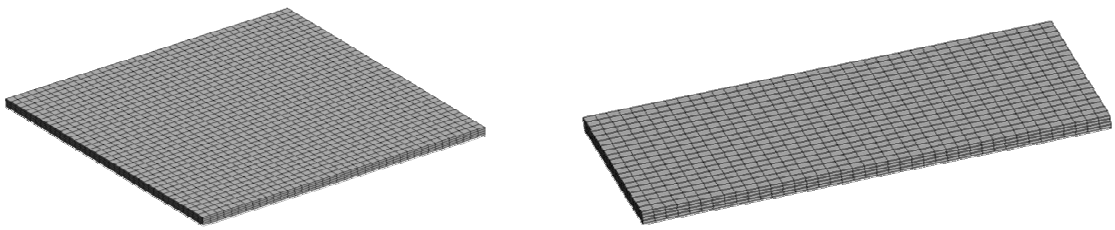

(a) (b)

Figure 13: Mesh of slabs: a) square and b) rectangular.

The distributed load *vs.* displacement curves at the centre of the spans of both slabs are respectively shown in Figure 14. Here, it may be observed that the intensity of the distributed load on clamped slabs are approximately five times greater than the intensity on simple supported slabs at the displacements of 2.5 and 0.5 cm, respectively. Additionally, it is observed that, for simple supported slabs, the ultimate load computed with the yield line theory is greater than the load computed with FEED; on the contrary, for clamped slabs, the ultimate load computed with the yield line theory is lower than the load computed with FEED. In simple supported slabs, this effect is attributed to the steel reinforcement placed at the centre of the span reaches the yield stress before the steel reinforcement placed at the edges does; whereas in the yield line theory, it is assumed that every bar instantly reaches the yield stress.

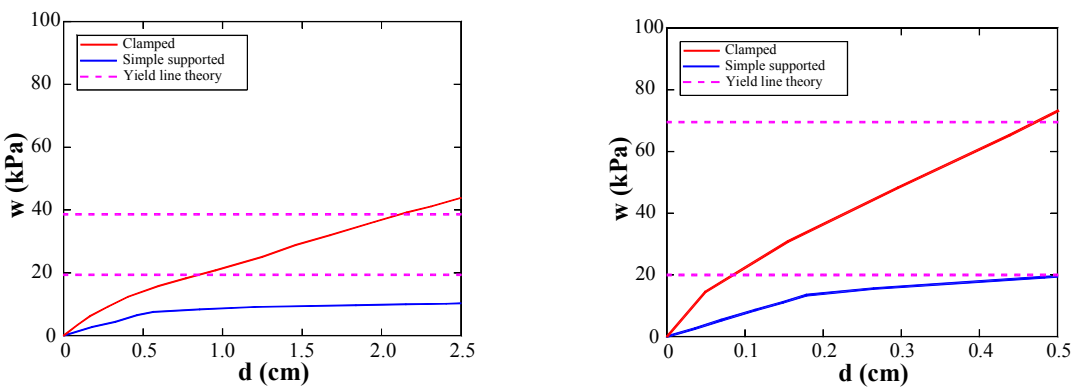

(a) (b)

Figure 14: Distributed load vs. displacement curves in slab: a) square and b) rectangular.

In the clamped square slab, cracking simultaneously initiated along the edges on the top surface, growing to the centre until a ring is formed, as shown in Figure 15a, whereas on the bottom surface, cracking paths form a kind of cross, growing to the corners and to the edges, as shown in Figure 15b. In the simple supported condition, cracking initiated at the corners and at the centre on the bottom surface, growing as shown in Figure 16b, whereas on top surface, it initiated at the corners, growing to the centre, as shown in Figure 16a.

In the clamped rectangular slab, cracking simultaneously initiated along its long edges on the top surface. Then, cracking appeared along its short edges, growing to the centre until a ring is formed as shown in Figure 17a. On the bottom surface, cracking initiated along a strip at the centre of the span, parallel to the long edges, growing to the corners and to the edges, as shown in Figure 17b. In the simple supported rectangular slab, cracking initiated along a strip at the centre on the bottom surface, parallel to the long edges as shown in Figure 18b; some cracks appeared at the corners on the top surface, as shown in Figure 18a. In general, the cracking paths on the bottom surfaces of the corresponding studied slabs were similar to the paths proposed by the classical yield line theory as well as the experimental results reported by Bach and Graf (1915).

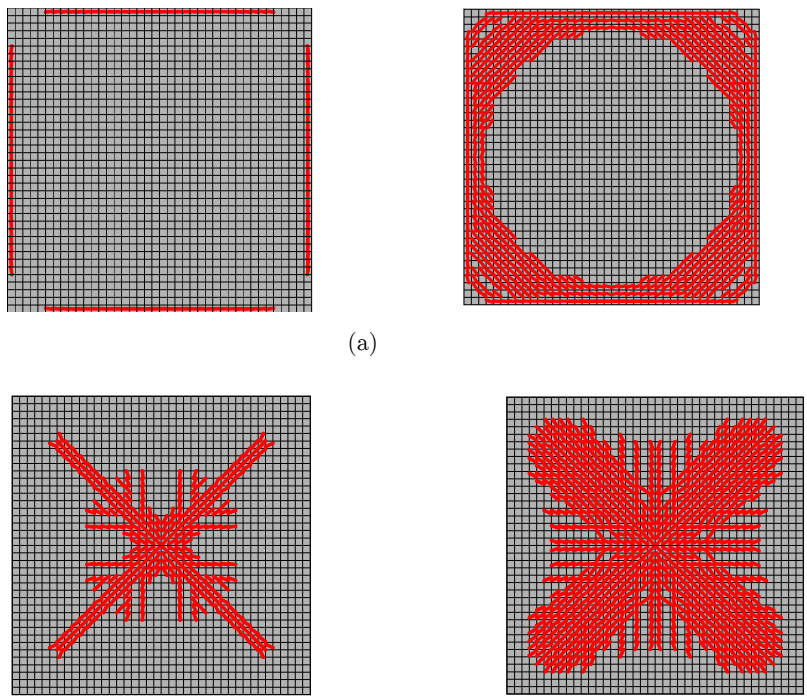

Figure 15: Cracking propagation of a clamped square slab on the: a) top and b) bottom surfaces.

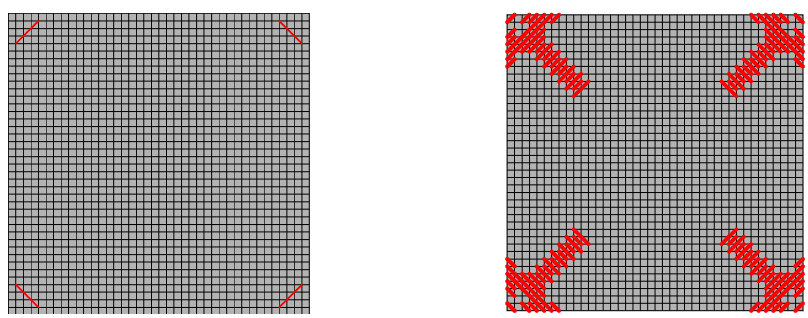

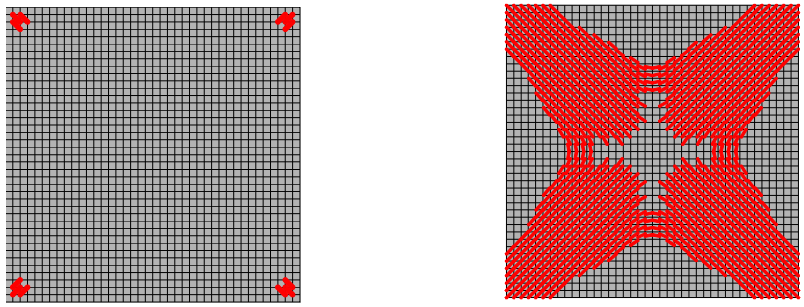

(b)

Figure 16: Cracking propagation of a simple supported square slab on the: a) top and b) bottom surfaces.

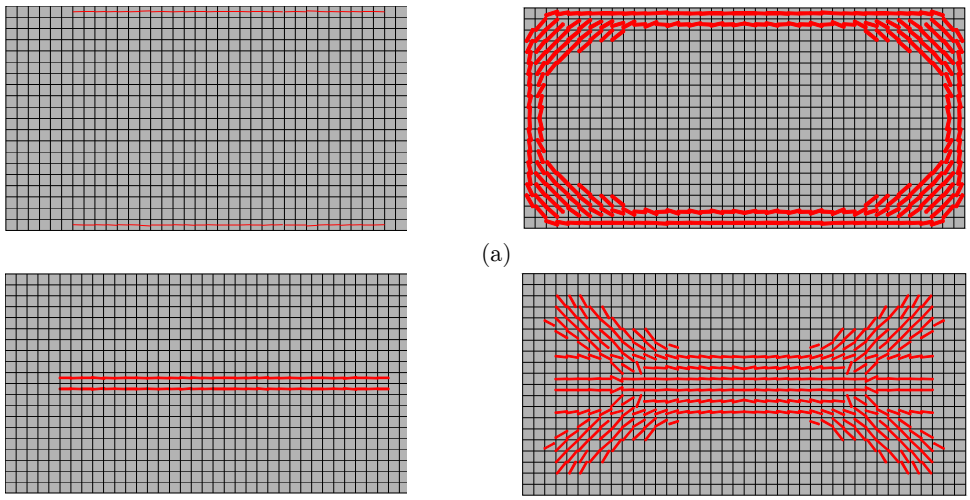

(a)

(b)

Figure 17: Cracking propagation of a clamped rectangular slab on the: a) top and b) bottom surfaces.

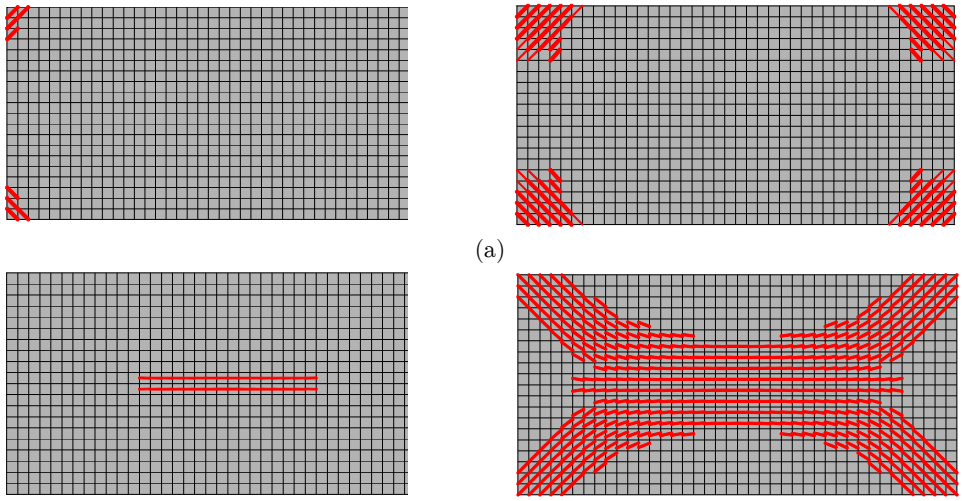

(a)

(b)

Figure 18: Cracking propagation of a simple supported rectangular slab on the: a) top and b) bottom surfaces.

To know if the steel reinforcement yields, the yield strain, $\varepsilon_y = \sigma_y/E_s = 0.0021$, was compared with the strains of the steel bars placed perpendicular to the central and edge strips of the slabs, *i.e.*, perpendicular to strips 0-A, 0-a, 0-B, A-C, a-c and b-c, respectively, as shown in Figure 10. The strains of the steel bars were only computed in half of the strips as they are symmetric.

In the clamped square slab, only the central reinforcing top steel bars placed perpendicular to the edge strip yielded as shown in

Figure 19b, while the other bars remained linear elastic as shown in

Figure **19**a. This result is congruent with the occurrence of cracking, which simultaneously initiated along the edges on the top surface. On the contrary, in the simple supported square slab, only the central reinforcing bottom steel bars placed perpendicular to the central strip yielded as shown in

Figure **20**a, while the other steel bars remained linear elastic as shown in

Figure **20**b. This result is also congruent with the occurrence of cracking, which initiated at the centre on the bottom surface.

In the clamped rectangular slab, only the central reinforcing top steel bars placed perpendicular to the long edge strip yielded, strip b-c, as shown in Figure 21c, while the other bars remained linear elastic as shown in Figure 21a, b and d. This result is congruent with the occurrence of cracking, which simultaneously initiated along the long edges on the top surface. On the contrary, in the simple supported rectangular slab, only the central reinforcing bottom steel bars placed perpendicular to the long central strip yielded, strip 0-a as shown in Figure 22a, while the other bars remained linear elastic as shown in Figure 22b, c and d. This result is also congruent with the occurrence of cracking, which initiated at the centre on the bottom surface.

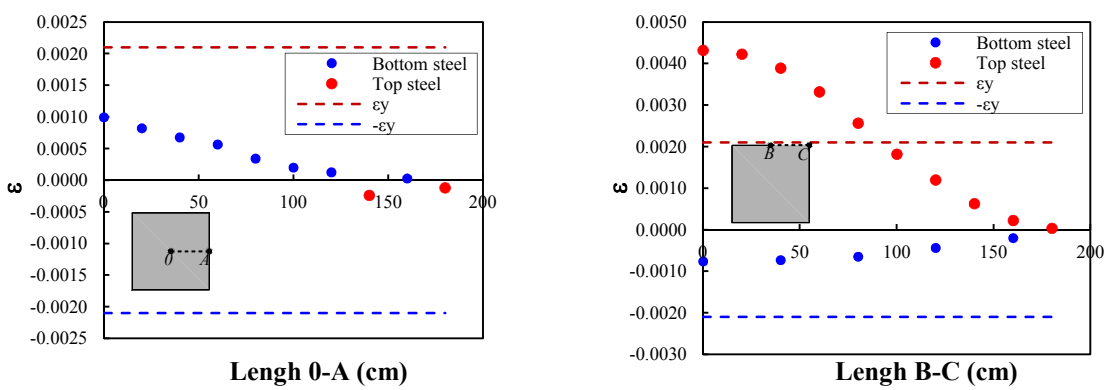

Figure 19: Strains in the reinforcing steel bars of the clamped square slab placed perpendicular to the: a) central strip 0-A and b) edge strip B-C.

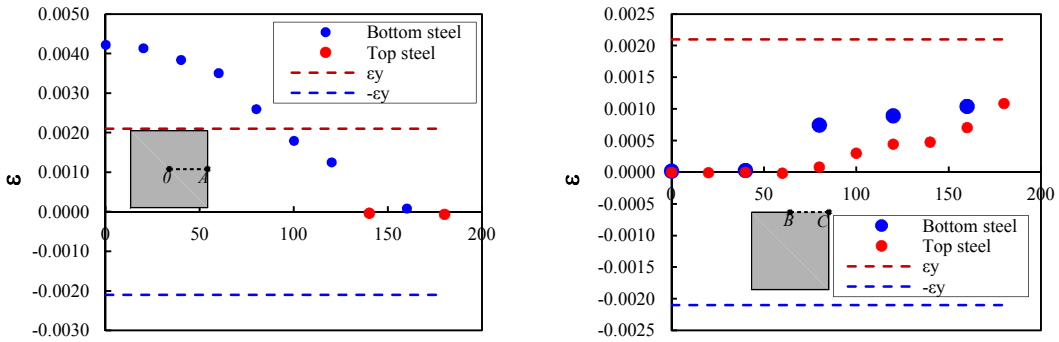

(a) (b)

Figure 20: Strains in the reinforcing steel bars of a simple supported slab placed perpendicular to the: a) central strip 0-A and b) edge strip B-C.

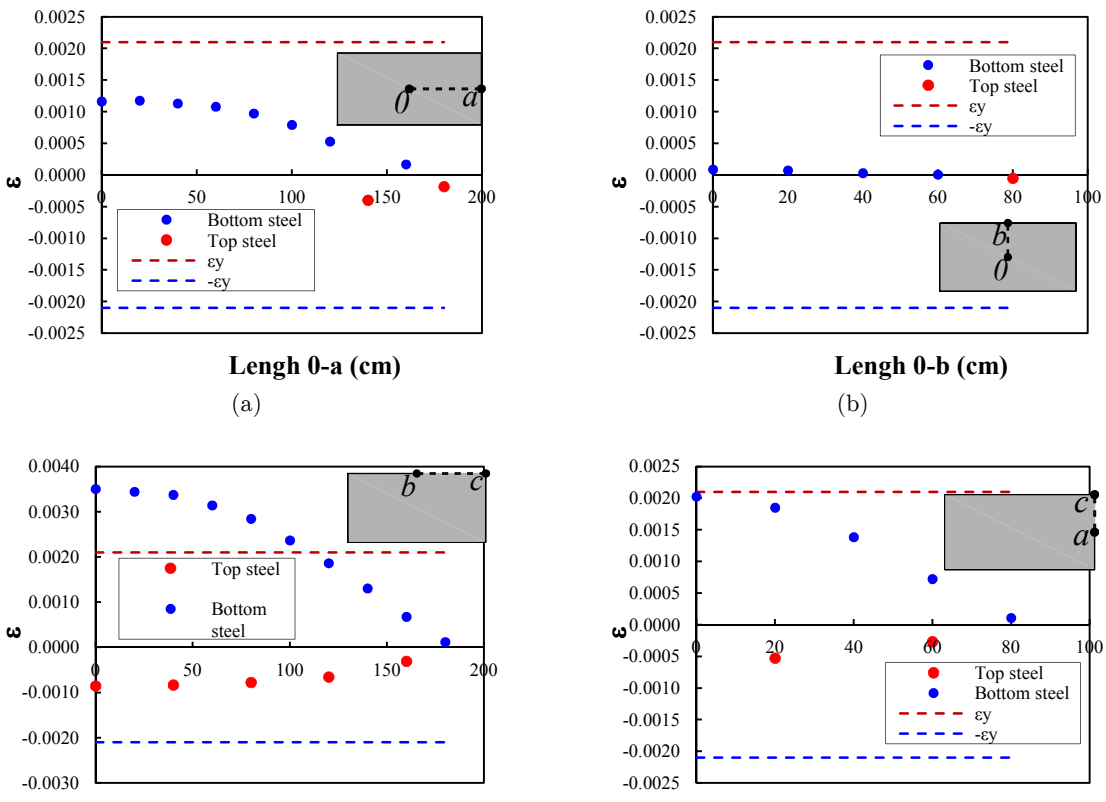

(a) (b) (c) (d)

Figure 21: Strains in the reinforcing steel bars of a clamped rectangular slab placed perpendicular to the: a) central strip 0-a, b) central strip 0-b, c) edge strip b-c and c) edge strip a-c.

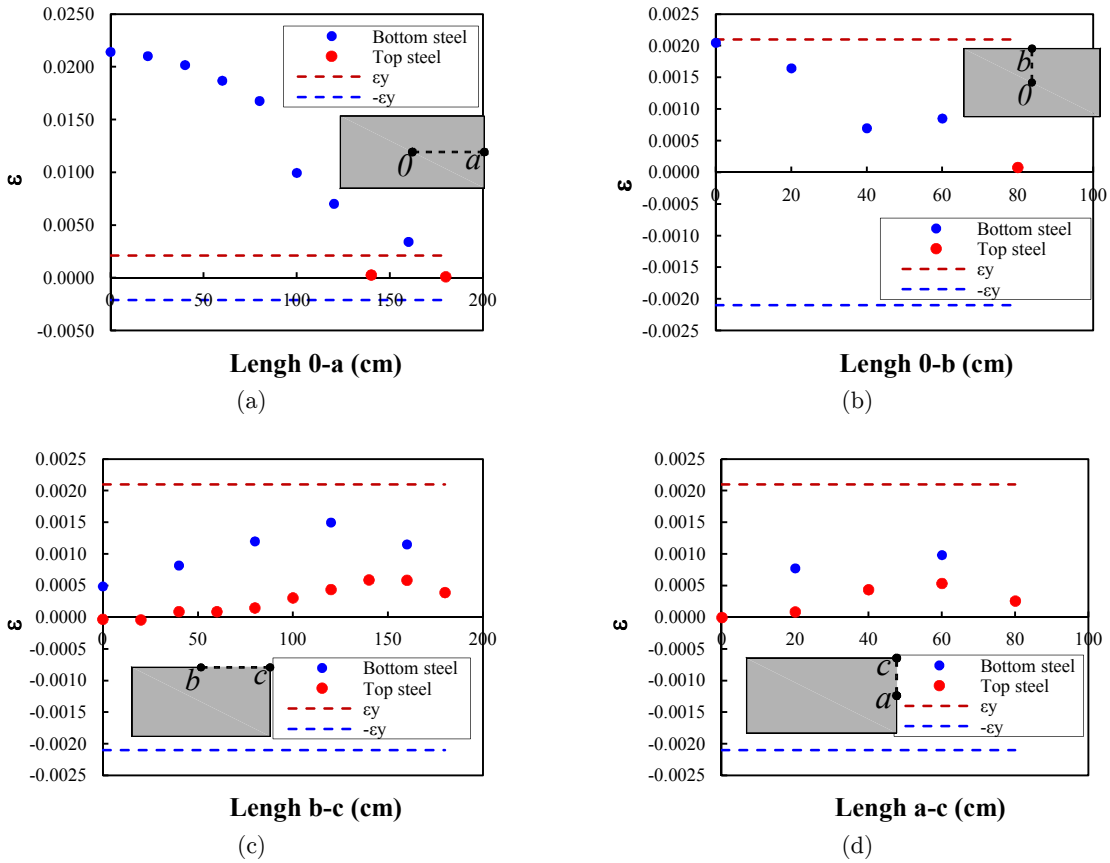

Figure 22: Strains in the reinforcing steel bars of a simple supported rectangular slab placed perpendicular to the: a) central strip 0-a, b) central strip 0-b, c) edge strip b-c and c) edge strip a-c.

5 CONCLUSIONS

The FEED with a discrete damage model were used for modelling concrete slabs under vertical load, involving their crack pattern and the load-displacement capacity curve. The discrete damage model considers a constitutive behaviour equipped with softening for the concrete elements limited for a damage surface, whereas for the reinforced concreted elements, a 1D rate independent plasticity model was assigned to the reinforcement, which take into account the hardening of the steel as isotropic.

The coupling of solid FEED and bar elements was validated with experimental results reported in the literature. Although the experimental curve shows a recovery of the displacement, it is considered that it was an effect of a slipping of the measurement equipment, since under an increasing vertical load it is not possible a recovery of the displacement at the centre of the span.

In clamped slabs, cracking initiated on the top surface at the centre of its edges, growing to the corners until a kind of ring is formed. On the bottom surface, cracking occurred at the centre of the span, propagating to the corners until a cross is formed. Whereas, in simple supported

slabs, cracking initiated at the centre of the span on the bottom surface, propagating to the corners until a cross was formed. On the top surface, incipient cracking occurred at the corners.

The ultimate load computed for simple supported slabs with the yield line theory is greater than the load computed with FEED; on the contrary, for clamped slabs, the ultimate load computed with the yield line theory is lower than the load computed with FEED. In simple supported slabs analysed with FEED, this effect is attributed that the steel reinforcement at the centre of the span reached the yield stress before the steel reinforcement placed at the edges did; whereas with the yield line theory, it is assumed that every bar instantly reaches the yield stress.

In the clamped square slab, the central reinforcing steel bars placed perpendicular to the edges yielded, while in the simple supported square slab the central reinforcing steel bars placed perpendicular to central strip yielded. On the other hand, in the clamped rectangular slab, the reinforcing steel bars placed perpendicular to the long edges yielded, while in the simple supported rectangular slab, the reinforcing steel bars placed perpendicular to long central strip yielded. These results were congruent with the places of the slabs where cracking initiated, corresponding to the places where grater tension stresses occurred.

Acknowledgements

The first author acknowledges the support given by the Universidad Autónoma Metropolitana and the financial support by CONACYT under the agreement number I010/176/2012, in the context of the research project: "Analysis and design of concrete slabs". The third author acknowledges the sponsorship by the General Directorate of Academic Personnel Affairs of UNAM of the PAPIIT project IN108512.

References

ABAQUS (2011). Example problems manual, Volumen1: static and dynamic analysis, Version 6.11, E.U.A., p.881.

Alfaiate, J., Simone, A., Sluys, L.J. (2003). Non-homogeneous displacement jumps in strong embedded discontinuities, International Journal of Solids and Structures 40 (21): 5799-5817.

ANSYS. (2010). ANSYS User's Manual version 13.0, ANSYS, Inc., Canonsburg, Pennsylvania, USA.

Bach, C., Graf, O. (1915). Versuche mit allseitig aufliegenden, quadratischen and rechteckigen eisenbetonplatten, Deutscher Ausschuss für Elsenbeton 30, Berlin. (In German)

Carpinteri, A. (1988). Cusp catastrophe interpretation of fracture instability, Journal of the Mechanics and Physics of Solids 37(5): 567-582.

Carpinteri, A., Carrado, M., Paggi M. (2010). An integrated cohesive/overlapping crack model for the analysis of flexural cracking and crushing in RC beams, International Journal of Fracture 161:161-173.

Casadei, P., Parretti, R., Nanni, A., Heinze, T. (2005). In situ load testing of parking garage reinforced concrete slabs: comparison between 24 h and cyclic load testing, ASCE Practice Periodical on Structural Design and Construction 10(1): 40-48.

Contrafatto, L., Cuomo, M., Di Venti, G.T. (2012). Finite Elements with non-homogeneous embedded discontinuities, In: 6th European Congress on Computational Methods in Applied Sciences and Engineering, ECCOMAS 2012, Vienna, Austria.

de Borst, R., Nauta, P. (1985). Non-orthogonal cracks in a smeared finite element model, Engineering Computations 2(1): 35-46.

DIANA (2008). DIANA 9.0: Finite Element Analysis User's Manual Release, TNO DIANA BV, Delft, Holanda.

Foster, S.J., Bauley, D.G., Burgess, I.W., Plank, R.J. (2004). Experimental behaviour of concrete floor slabs at large displacements, Engineering Structures 26(9): 1231-1247.

Galati, N., Nanni, A., Tumialan, J.G., Ziehl, P.H. (2008). In-situ evaluation of two concrete slab systems, I: load determination and loading procedure" ASCE Journal of Performance of Constructed Facilities 22(4): 207-216.

Gamble, W.L, Sozen, M.A., Siess, C.P. (1961). An experimental study of a two-way floor slab, Structural Research Series No. 211, Department of Civil Engineering, University of Illinois, p. 326.

Gilbert, R.I., Warner, R.F. (1978). Tension stiffening in reinforced concrete slabs. ASCE Journal of the Structural Division 104(12): 1885-1900.

Girolami, A.G., Sozen M.A., Gamble, W.L. (1970). Flexural strength of reinforced concrete slabs with externally applied in-plane forces, Report to the Department of Defense, Illinois University, Urbana, Illinois.

Hand, F.D., Pecknold, D.A., Schnobrich, W.C. (1973). Nonlinear analysis of reinforced concrete plates and shells, ASCE Journal of the Structural Division 99(7): 1491-1505.

Hatcher, D.S., Sozen, M.A, Siess, C.P. (1960). An experimental study of a quarter-scale reinforced concrete flat slab floor, Structural Research Series No. 200, Department of Civil Engineering, University of Illinois, p. 288.

Hatcher, D.S., Sozen, M.A., Siess C.P. (1961). A study of tests on a flat plate and a flat slab, Structural Research Series No. 217, Department of Civil Engineering, University of Illinois, p. 504.

Hinton, E., Abdel Rahman, H.H., Zienkiewicz, O.C., (1981). Computational strategies for reinforced concrete slab systems, International Association of Bridge and Structural Engineering, Colloquium on Advanced Mechanics of Reinforced Concrete: 303-313.

Jirsa, J.O., Sozen, M.A., Siess, C.P. (1962). An experimental study of a flat slab floor reinforced with welded wire fabric, Structural Research Series No. 248, Department of Civil Engineering, University of Illinois, p. 188.

Jofriet, J.C., McNeice, G.M. (1971). Finite element analysis of RC slabs, ASCE Journal of the Structural Division, 97 (3) 785-806.

Juárez, G., Ayala, G. (2009). Variational formulation of the material failure process in solids by embedded discontinuities model, Numerical Methods for Partial Differential Equations 25(1): 26-62.

Juárez-Luna, G., Ayala, G.A. (2014). Improvement of some features of finite elements with embedded discontinuities, Engineering Fracture Mechanics 118:31-48

Juárez-Luna G., Caballero-Garatachea O. (2014). Determinación de coeficientes de diseño y trayectorias de agrietamiento de losas aisladas circulares, elípticas y triangulares, Ingeniería Investigación y Tecnología XV(1):103-123. (In spanish)

Kabele, P., Cervenka, V., Cervenka, J. (2010). ATENA Program Documentation. Example Manual, ATENA Engineering, p. 90.

Kupfer, H.B., Gerstle, K.H. (1973). Behaviour of concrete under biaxial stresses, ASCE Journal of Engineering Mechanics 99 (4): 853-866.

Kwak, H.G., Filippou, F.C. (1990). Finite element analysis of reinforced concrete structures under monotonic loads, Department of Civil Engineering, University of California, Berkeley, California, p. 124.

Lin, C.S., Scordelis, A.C. (1975). Nonlinear analysis of RC shells of general form, ASCE Journal of the Structural Division 101(3): 523-238.

Lotfi, H.R., Shing, P. (1995). Embedded representation of fracture in concrete with mixed finite elements, International Journal for Numerical Methods in Engineering 38(8): 1307-1325.

Mayes, G.T., Sozen, M.A., Siess, C.P. (1959). Tests on a quarter-scale model of a multiple-panel reinforced concrete flat plate floor, Structural Research Series No. 181, Department of Civil Engineering, University of Illinois.

Mcneice, A.M. (1967). Elastic-plastic bending of plates and slabs by the finite element method, Dissertation, London University.

Oliver, J. (1996). Modelling strong discontinuities in solid mechanics via strain softening constitutive equations, Part 1: Fundamentals, 39(21): 3575-3600. Part 2: Numerical simulation, International Journal for Numerical Methods in Engineering 39(21): 3601-3623.

Park, R., Gamble, W.L. (2000). Reinforced concreted slabs, John Wiley & Sons, second edition.

Rots, J.G. (1988). Computational modeling of concrete fracture, Dissertation, Delft University of Technology, The Netherlands, p.132.

Sancho, J.M., Planas, J., Cendón, D.A., Reyes, E., Gálvez, J.C. (2007). An embedded crack model for finite element analysis of concrete fracture, Engineering Fracture Mechanics 74(1-2): 75-86.

Smadi, M.M., Belakhdar, K.A. (2007). Development of finite element code for analysis of reinforced concrete slabs, Jordan Journal of Civil Engineering 1(2): 202-219.

Taylor, L.R. (2008). A finite element analysis program (FEAP) v8.2, Department of Civil and Environmental Engineering, University of California at Berkeley, Berkeley, CA.

Vanderbilt, M.D., Sozen, M.A., Siess, C.P. (1961). An experimental study of a reinforced concrete two-way floor slab with flexible beams" Structural Research Series No. 228, Department of Civil Engineering, University of Illinois, p. 188.

Wang, Y., Dong, Y., Zhou G. (2013). Nonlinear numerical modeling of two-way reinforced concrete slabs subjected to fire, Computers & Structures 119(1): 23-36.

Wells, G.N., Sluys, L.J. (2001). A new method for modelling cohesive cracks using finite elements, International Journal for Numerical Methods in Engineering 50(12): 2667-2682.

Westergaard, H.M., Slater, W.A. (1921). Moments and stresses in slabs, Proc. of the American Concrete Institute 17 (2): 415-538.